SCIENTIFIC REPORTS

Hexagonal 2H-MoSe$_2$ broad spectrum active photocatalyst for Cr(VI) reduction

Haipeng Chu[1], Xinjuan Liu[1], Baibai Liu[1], Guang Zhu[2], Wenyan Lei[1], Huigang Du[1], Junying Liu[3], Jianwei Li[4], Can Li[1] & Changqing Sun[1]

To make full use of the solar energy, exploring broad spectrum active photocatalysts has become one of the core issues for photocatalysis. Here we report a novel hexagonal 2H-MoSe$_2$ photocatalyst with ultraviolet (UV)-visible-near infrared (NIR) light response for the first time. The results indicate that the MoSe$_2$ displays excellent photo-absorption and photocatalytic activity in the reduction of Cr(VI) under UV and visible even NIR light irradiation. MoSe$_2$ synthesized at pH value of 2 achieves the highest Cr(VI) reduction rates of 99%, 91% and 100% under UV, visible and NIR light irradiation, respectively, which should be attributed to its comparatively higher light absorption, efficient charge separation and transfer as well as relatively large number of surface active sites. The excellent broad spectrum active photocatalytic activity makes the MoSe$_2$ to be a promising photocatalyst for the effective utilization of solar energy.

Agrowing number of contaminations such as heavy metal ions and organic chemical compounds in natural water have become a serious threat to environment and human health. Hexavalent chromium (Cr(VI)) is a most common contaminant, which is discharged from industries such as electroplating, leather tanning, metal finishing, textile manufacturing, steel fabricating, paint and pigments, fertilizing, and so on. It is highly toxic to most organisms when its concentration is above 0.05 mg l^{-1}, and can cause the lung-cancer, chromeulcer, perforation of nasal septum and kidney-damage. Various techniques, such as adsorption, biosorption, electrocoagulation, ion exchange, membrane filtration, have been reported to remove the Cr(VI) from wastewater[1,2]. However, these techniques have some disadvantages, such as membrane fouling, high power consumption and cost for operation and maintenance.

The reduction of Cr(VI) to Cr(III) is considered as an efficient route to remove Cr(VI), because Cr(III) is less toxic and can be readily precipitated in aqueous solution in the form of Cr(OH)$_3$[3]. Semiconductor photocatalysis as a novel, economical and environmentally-friendly technique for the reduction of Cr(VI) has attracted considerable attention in recent years[4–7]. One of the major factors in photocatalysis is the limited light absorption of photocatalysts in the incident solar spectrum. Up to now, most of the photocatalysts such as TiO$_2$, CuO, CdS, SnS$_2$, AgCl:Ag, WO$_3$ and metal-free g-C$_3$N$_4$ *et al.* are only active under ultraviolet (UV) or visible light irradiation[8–22]. UV and visible light make up only about 4% and 43% of the solar energy reaching the surface of the earth, respectively, while near-infrared (NIR) light constitutes more than 50%[23–25]. Nevertheless, up to now few efforts have been made to effectively utilize the NIR light[26–28]. Therefore, exploration of novel broad spectrum (UV, visible and NIR) responsive semiconductors with efficient and stable photocatalytic activity remains a challenge.

Transition metal dichalcogenides (TMDs) have attracted great interests due to their intriguing properties and potential applications in hydrogen evolution[29], lithium/sodium batteries[30], and photocatalysis[31–34]. Among these TMDs, MoSe$_2$ with a narrow band gap of ~1.4 eV can harvest the solar energy in a very broad spectral region and has been employed as an efficient photocatalyst under UV, visible and NIR light irradiation[35]. Theoretical studies indicated that single layer MoSe$_2$ is an ideal candidate for photocatalytic splitting of water to generate hydrogen

[1]Institute of Coordination Bond Metrology and Engineering, College of Materials Science and Engineering, China Jiliang University, Hangzhou 310018, China. [2]Anhui Key Laboratory of Spin Electron and Nanomaterials, Suzhou University, Suzhou 234000, China. [3]Research Center for Combustion and Environment Technology, Shanghai Jiao Tong University, Shanghai 200240, China. [4]Jiangsu Key Laboratory of Advanced Laser Materials and Devices, Hydrogen energy laboratory, Laboratory for Quantum Design of Functional Material, School of Physics and Electronic Engineering, Jiangsu Normal University, Xuzhou 221116, China. Correspondence and requests for materials should be addressed to X.L. (email: lxj669635@126.com)
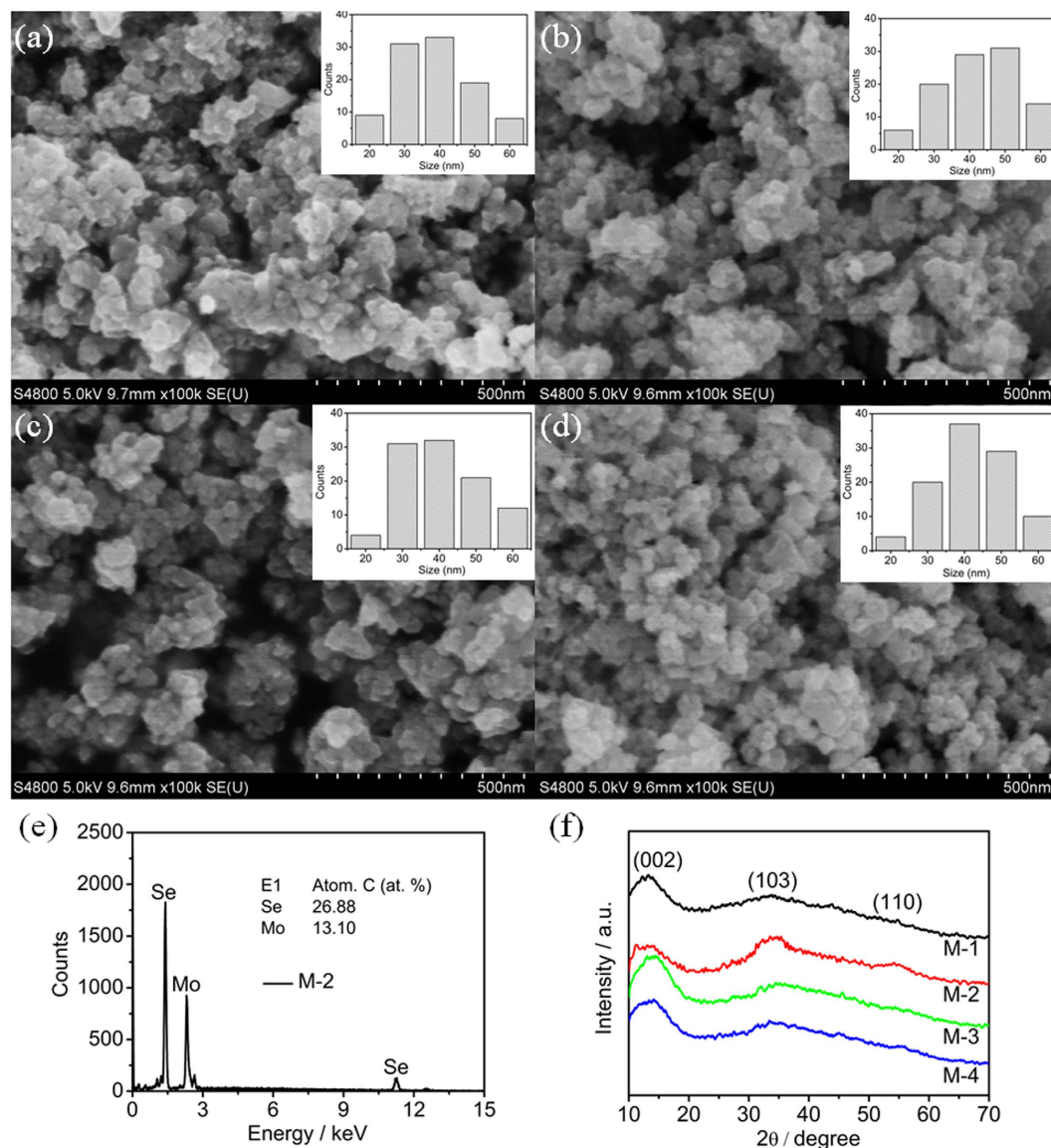
Figure 1. FESEM images of (**a**) M-1, (**b**) M-2, (**c**) M-3 and (**d**) M-4; (**e**) EDS spectrum and (**f**) XRD pattern of M-2. Scale bars: (**a–d**) 500 nm. Inset is the particle size distribution of (**a**) M-1, (**b**) M-2, (**c**) M-3 and (**d**) M-4.

in solar light irradiation[36]. So far, previous studies focused mainly on the visible light photocatalytic activity of $MoSe_2$ in the degradation of dye. Unfortunately, there have been no reports on the photocatalytic activity of $MoSe_2$ under UV and NIR light irradiation, especially for photocatalytic reduction of Cr(VI).

In this work, novel broad spectrum responsive $MoSe_2$ was synthesized via a facile solvothermal method for the first time. The $MoSe_2$ exhibits excellent photo-absorption in the whole light region and shows good photocatalytic activity in the reduction of Cr(VI) under UV, visible and NIR light irradiation. The photocatalytic mechanism was also studied in terms of a series of characterization and controlled experiments using hole scavengers.

Results and Discussion

Characterizations of $MoSe_2$. Figure 1 shows the field-emission scanning electron microscopy (FESEM) images of M-1, M-2, M-3 and M-4. It is clearly observed that all the $MoSe_2$ samples display the nanoparticle structures with a size range between 30 and 50 nm (inset of Fig. 1a–d), which indicates that the morphology of $MoSe_2$ does not change when the pH value of the precursor solution increases from 1 to 4. However, the $MoSe_2$ nanoparticles are aggregated when the pH value increases to 3 and 4. The M-2 was identified by energy dispersive X-ray spectroscopy (EDS) linked to FESEM, as shown in Fig. 1e. The atom ratio of Mo and Se is about 1:2, further indicating the formation of $MoSe_2$. Figure 1f shows the X-ray diffraction (XRD) patterns of M-1, M-2, M-3 and M-4. The diffraction patterns of as-prepared $MoSe_2$ samples show that all the peaks can be indexed to (002), (102) and (110) crystal planes of the hexagonal 2H-$MoSe_2$ phase with space group $P6_3/mmc$ (JCPDS: 29–0914)[37]. No other impurity peaks for as-prepared $MoSe_2$ samples are observed, which confirms that the as-prepared products are pure $MoSe_2$. The XRD pattern of commercial $MoSe_2$ (labeled as $MoSe_2$ bulk) was also measured for comparison,
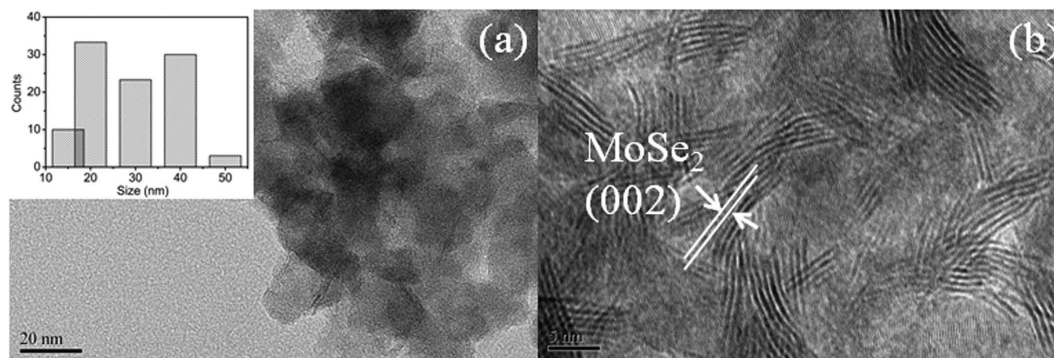
Figure 2. (**a**) Low-magnification and (**d**) high-magnification HRTEM images of M-2. Scale bars: (**a**) 20 nm and (**b**) 5 nm. Inset is the particle size distribution of (**a**) M-2.
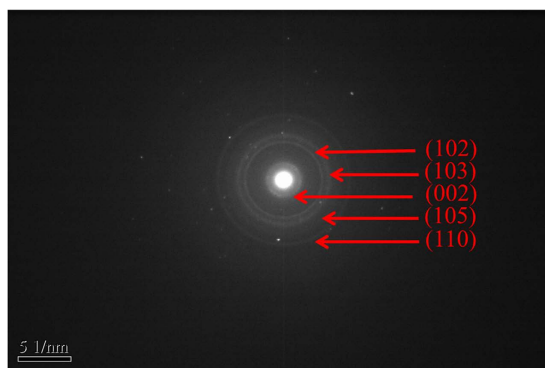

Figure 3. SAED pattern of M-2. Scale bars: 5 1/nm.

as shown in Figure S1. It can be observed that the XRD patterns of as-prepared $MoSe_2$ samples show relatively broader diffraction peaks compared with $MoSe_2$ bulk, indicating that the as-prepared products are somewhat amorphous and have short range structural order[38]. This is in good agreement with the reported results[39]. The crystallinity does not play a decisive role in the optical and photocatalytic activity of $MoSe_2$. In addition, the diffraction peaks of as-prepared $MoSe_2$ samples shift toward smaller angle, suggesting their larger interlayer spacing than that of the $MoSe_2$ bulk.

Figure 2a,b show the high-resolution transmission electron microscopy (HRTEM) images of M-2. The morphologies of M-1, M-3 and M-4 (not shown here) are similar to that of M-2. $MoSe_2$ nanoparticles are monodisperse with the diameters in the range of 30–50 nm (inset of Fig. 2). Furthermore, it is clearly observed from Fig. 2b that the $MoSe_2$ nanoparticles are formed by self-assembly nanosheets. Commonly, the $MoSe_2$ appears to have a 2D sheet-like structure with abundant active defective-edges, but the defects can act as recombination center instead of providing an electron pathway and promote the recombination of electron-hole pairs[40]. Compared with $MoSe_2$ with 2D sheet-like structure, the defects of $MoSe_2$ nanoparticles formed by self-assembly nanosheets are relatively less, which is beneficial to the photocatalytic activity. The interlayer spacing of 0.68 nm observed from lattice fringes can be ascribed to the (002) direction of hexagonal $MoSe_2$, which is slightly larger than that of the $MoSe_2$ bulk (0.64 nm). This result is in agreement with the XRD result. The selected area electron diffraction (SAED) pattern in Fig. 3 shows clear diffraction rings and can be well indexed as a pure hexagonal $MoSe_2$ phase, indicating a high crystallinity of $MoSe_2$.

In order to investigate the chemical composition of M-2, X-ray photoelectron spectroscopy (XPS) measurements were carried out. Figure 4a, b show the high resolution XPS spectra of Mo 3d and Se 3d for M-2. Mo $3d_{5/2}$ and Mo $3d_{3/2}$ were found at 228.7 eV and 232.4 eV, respectively, revealing the chemical oxidation state of $+4$ for Mo and the formation of $MoSe_2$[41]. The peak at 55 eV is attributed to Se $3d_{3/2}$. The mole ratio of Mo:Se in M-2 is about 1:2, further indicating the high purity of the products, which is in accordance with the EDS measurement. The XPS spectra of M-1, M-3, M-4 and $MoSe_2$ bulk (Figure S1) are similar to that of M-2. Compared with $MoSe_2$ bulk, the binding energies of Mo 3d and Se 3d for as-prepared $MoSe_2$ show a blue shift, which may be due to atomic undercoordination induced local quantum entrapment and polarization[42]. All of these results clearly confirm the formation of $MoSe_2$ photocatalyst.

Ultrahigh photocatalytic activity.   Photocatalytic reduction of Cr(VI) by M-1, M-2, M-3 and M-4 was performed under NIR light irradiation. Figure 5 shows the UV-vis absorption spectra of Cr(VI) with irradiation time under NIR light irradiation using M-2. It is observed that the UV-vis absorption of Cr(VI), related to its concentration in the solution, becomes weak with the increase in the irradiation time.
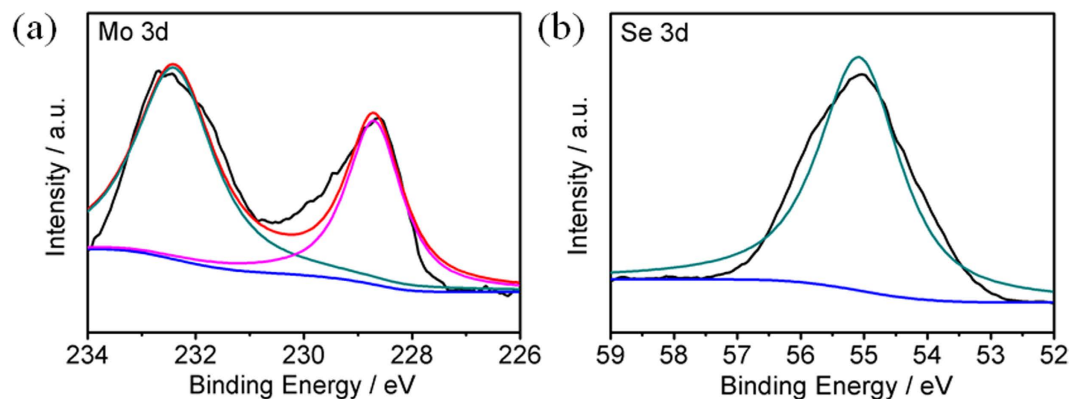
Figure 4. High-resolution XPS spectra of (**a**) Mo 3d and (**b**) Se 3d for M-2.
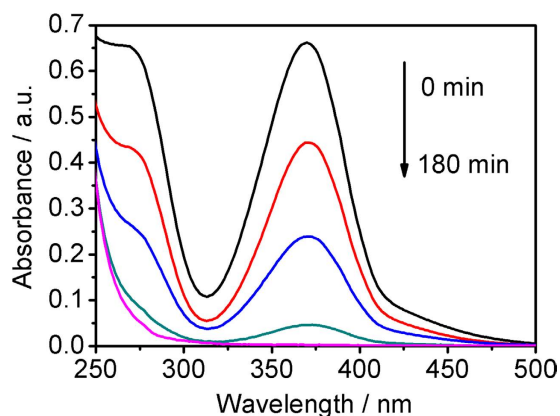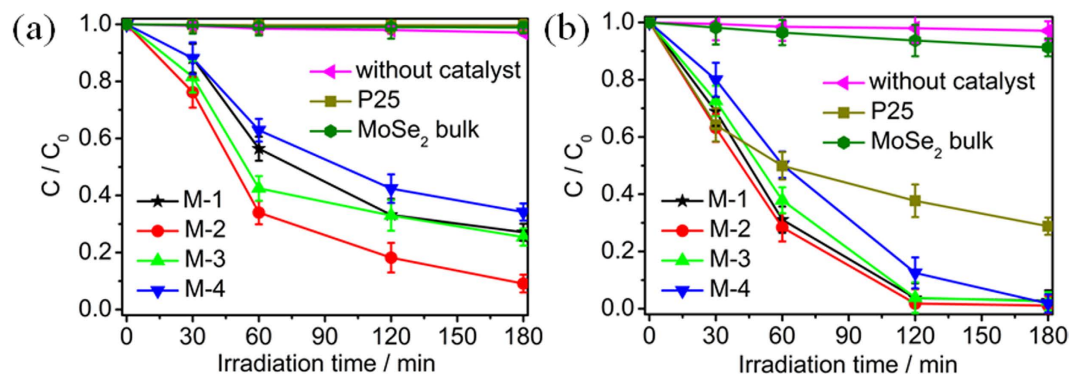

Figure 5. UV-vis absorbance of Cr(VI) with the variation of NIR light irradiation time.
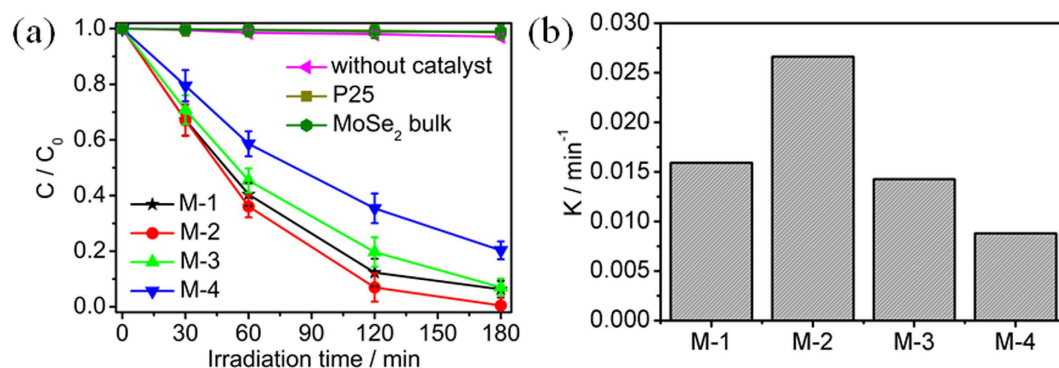

Figure 6. (**a**) Photocatalytic reduction of Cr(VI) by P25, MoSe$_2$ bulk, M-1, M-2, M-3 and M-4 under NIR light irradiation; and (**b**) photocatalytic reaction kinetics of Cr(VI) with reaction time.

Figure 6a displays the time-dependent reduction rates of Cr(VI) by P25, MoSe$_2$ bulk, M-1, M-2, M-3 and M-4 under NIR light irradiation. The normalized temporal concentration changes (C/C_0) of Cr(VI) during the photocatalytic process are proportional to the normalized maximum absorbance (A/A_0), which can be derived from the change in the Cr(VI) absorption profile during the photocatalysis process. It is observed that the concentration of Cr(VI) is hardly reduced under NIR light irradiation in the absence of the photocatalyst. The reduction rates of Cr(VI) for P25 and MoSe$_2$ bulk are 1% and 1%, respectively. The photocatalytic activity of MoSe$_2$ is dependent on the pH value of precursor solution. The reduction rate of Cr(VI) for M-1 is 94% at 180 min. When the pH value of precursor solution increases to 2, the reduction rate increases and reaches a maximum value of 100% for M-2 at 180 min. However, when the pH value of precursor solution further increases, the reduction rate decreases to 93% and 80% for M-3 and M-4 at 180 min, respectively. Figure 6b shows the linear fitting between pseudo-first-order kinetic equation and experimental data for P25, MoSe$_2$ bulk, M-1, M-2, M-3 and M-4. The values of rate constants

Figure 7. Photocatalytic reduction of Cr(VI) by P25, MoSe$_2$ bulk, M-1, M-2, M-3 and M-4 under (**a**) visible and (**b**) UV light irradiation.
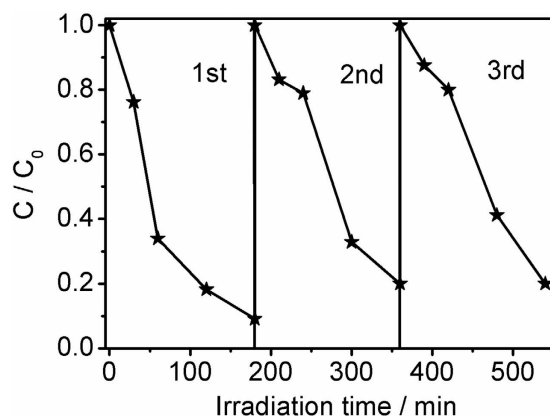

Figure 8. Photo-stability of M-2 by investigating its photocatalytic activity with three times of cycling uses.

(k) can be obtained directly from the fitted straight-line plots of $\ln(C/C_0)$ versus reaction time. It is observed that the values of k are very low (0.0002 min^{-1} for the absence of the photocatalyst; 0.0007 min^{-1} for P25 and MoSe$_2$ bulk) under NIR light irradiation). The value of k under NIR light irradiation follows the order: M-2 (0.0267 min^{-1}) > M-1 (0.0159 min^{-1}) > M-3 (0.0143 min^{-1}) > M-4 (0.009 min^{-1}). The result shows that M-2 exhibits a best photocatalytic activity under NIR light irradiation.

Photocatalytic reduction of Cr(VI) by P25, MoSe$_2$ bulk, M-1, M-2, M-3 and M-4 was also performed under visible and UV light irradiation, as shown in Fig. 7. Under visible light irradiation, the reduction rates of Cr(VI) for P25, MoSe$_2$ bulk, and M-1 are 1%, 1% and 73%, respectively, and a maximum reduction rate reaches 91% for M-2 at 180 min. However, when the pH value of precursor solution further increases, the reduction rate decreases to 75% and 66% for M-3 and M-4 at 180 min, respectively. Under UV light irradiation, the reduction rates are 71%, 9%, 97%, 99%, 97% and 97% for P25, MoSe$_2$ bulk, M-1, M-2, M-3 and M-4, respectively. Therefore, MoSe$_2$ can exhibit excellent photocatalytic activity not only under NIR light irradiation but also under UV and visible light irradiation.

The photo-stability of photocatalysts is very important for practical application. Therefore, the photo-stability of MoSe$_2$ (M-2) was studied by investigating its photocatalytic activity under visible light irradiation with three times of cycling uses, as shown in Fig. 8. It is noteworthy that only insignificant decrease for photocatalytic activity is found, which may be due to the loss of photocatalyst during collection process. Moreover, the crystal structure of M-2 after the photocatalytic reaction was characterized by XRD and XPS (Figures S3 and S4). It can be observed from the XRD pattern that the crystal structure of M-2 does not show an obvious change before and after the photocatalytic reaction. The XPS spectrum of Mo 3d for M-2 after the photocatalytic reaction displays two peaks at 228.7 eV and 232.4 eV, assigned to Mo 3d$_{5/2}$ and Mo 3d$_{3/2}$, respectively. A characteristic peak located at 55 eV can be observed in Figure S2b, corresponding to Se 3d$_{3/2}$. All of these results clearly confirm the good photo-stability of MoSe$_2$ photocatalyst under the studied conditions.

Mechanism of Photocatalytic Activity. During photocatalysis, the adsorption of Cr(VI), light absorption as well as the charge transportation and separation are crucial factors[43,44]. Figure 9 displays the nitrogen adsorption-desorption isotherms of M-1, M-2, M-3 and M-4. It can be observed that all of them show type IV isotherms with H3 hysteresis loop. The specific surface areas, pore sizes and pore volumes of M-1, M-2, M-3 and M-4 are listed in Table S1. The result shows that the specific surface area is almost same at low pH values of 1 and 2, while it decreases obviously when the pH value increases to 3 and 4, which may be due to the aggregation of
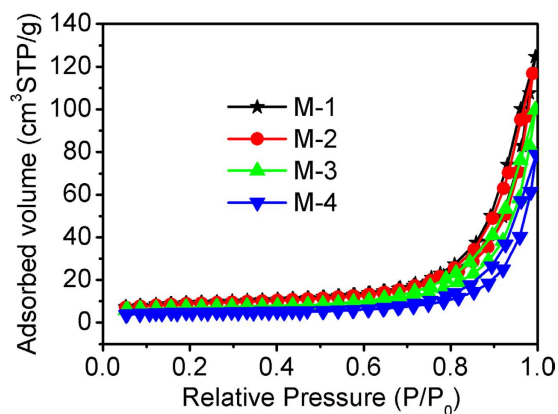
Figure 9. Nitrogen adsorption-desorption isotherms of M-1, M-2, M-3 and M-4.
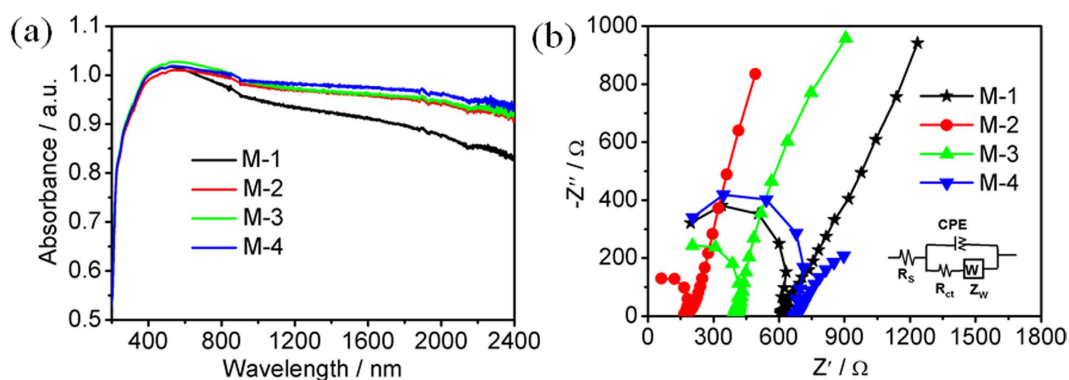

Figure 10. (**a**) UV-Vis-NIR diffuse absorption spectra and (**b**) Nyquist plots of M-1, M-2, M-3 and M-4. Inset of b is the corresponding equivalent circuit model.

MoSe$_2$ nanoparticles. The pore volumes of M-1 and M-2 are larger than those of M-3 and M-4. Larger specific surface area and pore volume can allow more Cr(VI) to enter into the MoSe$_2$, which is beneficial to the photocatalytic activity[45]. The pore size of MoSe$_2$ increases with the pH value of precursor solution increases, which can influence the fast transport of Cr(VI), but it does not play a decisive role in the photocatalytic activity of MoSe$_2$.

Figure 10a shows the UV-Vis-NIR diffuses absorption spectra of M-1, M-2, M-3 and M-4. It can be observed that all MoSe$_2$ samples exhibit strong absorption in the entire visible light and even NIR light region. Compared with M-1, M-2, M-3 and M-4 have better absorption. Highly ordered mesoporous crystalline MoSe$_2$ synthesized using mesoporous silica SBA-15 as a hard template via a nanocasting strategy was found to show a strong absorption band covering from 400–800 nm[35], suggesting that the highly ordered mesoporous crystalline MoSe$_2$ can only absorb the visible light. Furthermore, the diffuse reflectance spectra were also used to estimate the band gap energy through the Kubelka-Munk function: $F(R) = \alpha = (1-R)^2/2R$, where R is the percentage of reflected light and α is absorption coefficient, as shown in Figure S5a. The indirect band gap of all MoSe$_2$ samples are determined by extrapolating the linear portion of $(\alpha h v)^{1/2}$ plot (Figure S5b). The absorption edges and band gap energies of all MoSe$_2$ samples are about 984 nm and 1.26 eV, respectively.

The charge transfer and recombination behavior of the as-prepared samples was studied by analyzing the electrochemical impedance spectra (EIS) spectra in dark condition. Figure 8b shows the typical Nyquist plots of M-1, M-2, M-3 and M-4. The semicircle in the EIS spectra is ascribed to the contribution from the charge transfer resistance (R_{ct}) and constant phase element (CPE) at the photocatalyst/electrolyte interface. The inclined line, resulting from the Warburg impedance Z_W, corresponds to the ion-diffusion process in the electrolyte. The corresponding equivalent circuit is shown in the inset of Fig. 10b. The fitted R_s, R_{ct}, CPE and Z_W for all MoSe$_2$ samples are listed in Table S2. It is found that the R_{ct} for M-2 is 143.3 Ω, much lower than those for other MoSe$_2$ samples, indicating that the recombination of photo-induced electrons and holes in M-2 is more effectively inhibited. The results confirm that the pH value of the precursor solution can influence the charge transfer and recombination behavior.

The charge separation and transfer behavior of the as-prepared samples was also investigated by photoluminescence (PL) and photoelectronchemical measurements. Figure S6a shows PL spectra of M-1, M-2, M-3 and M-4 with the excitation wavelength of 320 nm. It can be clearly observed that the intensity of M-2 is much weaker than those of other MoSe$_2$ samples, which further confirms that the recombination of photo-induced electrons and holes in M-2 can be effectively inhibited. Figure S6b shows the time resolved PL (TRPL) spectra of M-1,
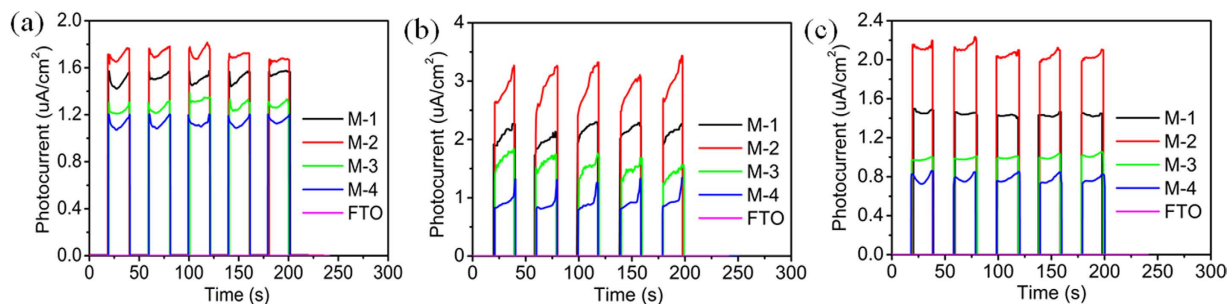
Figure 11. Transient photocurrent responses of M-1, M-2, M-3 and M-4 without bias versus Ag/AgCl under (**a**) UV, (**b**) visible and (**c**) NIR light irradiation.
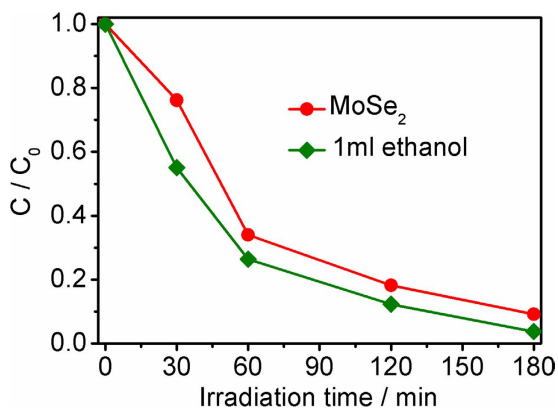

Figure 12. Photocatalytic reduction of Cr(VI) by M-2 with the addition of hole scavenger under visible light irradiation.

M-2, M-3 and M-4. The decay curves were fitted by exponentials to obtain the decay time. The average lifetimes of charge carriers are calculated to be 0.29, 0.34, 0.27 and 0.17 ns for M-1, M-2, M-3 and M-4, respectively. M-2 shows the longest lifetime, which can improve the charge separation and transfer efficiency, and thus enhance the photocurrent[22]. Figure 11 shows the transient photocurrent responses of M-1, M-2, M-3 and M-4 under UV, visible and NIR light irradiation in the photocatalytic reaction. It can be observed that the photocurrent quickly decreases to zero when the light is switched off, indicating the recombination of photo-induced electron and hole. M-2 exhibits the highest photocurrent, revealing more efficient charge transfer process and longer lifetime of the photo-induced electron-hole pairs. All results are in agreement with the EIS results.

It is known that during photocatalysis, the adsorption of pollutants, the light harvesting as well as the charge transportation and separation are crucial factors[46]. Compared with M-1, M-2, M-3 and M-4 show a higher absorption, resulting in an increase of the number of photo-generated electrons and holes. Compared with M-3 and M-4, M-2 shows larger specific surface area and pore volume, which is beneficial for adsorbing the Cr(VI). In addition, M-2 exhibits the lowest resistance and highest photocurrent, indicating that the recombination of photo-induced electrons and holes in M-2 is most effectively inhibited. All results are beneficial to the enhanced photocatalytic activity, which has been confirmed by the UV-Vis-NIR absorption, EIS and BET measurements. Therefore, among all samples, M-2 exhibits the best photocatalytic activity under UV, visible and NIR light irradiation.
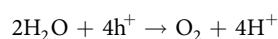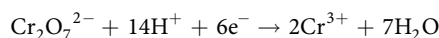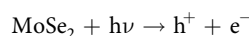
To confirm the role of the photo-generated electrons in the photocatalytic process, controlled experiments were carried out with addition of hole scavenger (ethanol). As shown in Fig. 12, the photocatalytic activity of M-2 is enhanced with the addition of hole scavenger in that the ethanol as hole scavenger can capture photo-generated holes in the photocatalytic process, and thus suppresses the recombination of photo-generated carriers. The results indicate that the photo-generated electrons govern this photocatalytic process, which is consistent with the report in the literature[47].

Based on the above analysis, the possible photocatalytic mechanism of $MoSe_2$ in the reduction of Cr(VI) is proposed. In the process, $MoSe_2$ is excited under UV, visible or NIR light irradiation, and thus the electron-hole pairs are generated. The photo-generated charge carriers may migrate to the surface of $MoSe_2$ and participate in the reduction and oxidation reactions. The valance band (VB) of all $MoSe_2$ samples was measured by ultraviolet photoelectron spectroscopy (UPS) measurement, as shown in Fig. 13a. It can be observed that the VB values of M-1, M-2, M-3 and M-4 are 0.46, 0.26, 0.52, and 0.64 V (*vs.* normal hydrogen electrode (NHE)), respectively. The conduction bands (CB) are calculated to be −0.8, −1.0, −0.74, and −0.62 V (*vs.* NHE) corresponding to M-1, M-2, M-3 and M-4, respectively. The energy level structures of all $MoSe_2$ samples are provided in Fig. 13b. Because
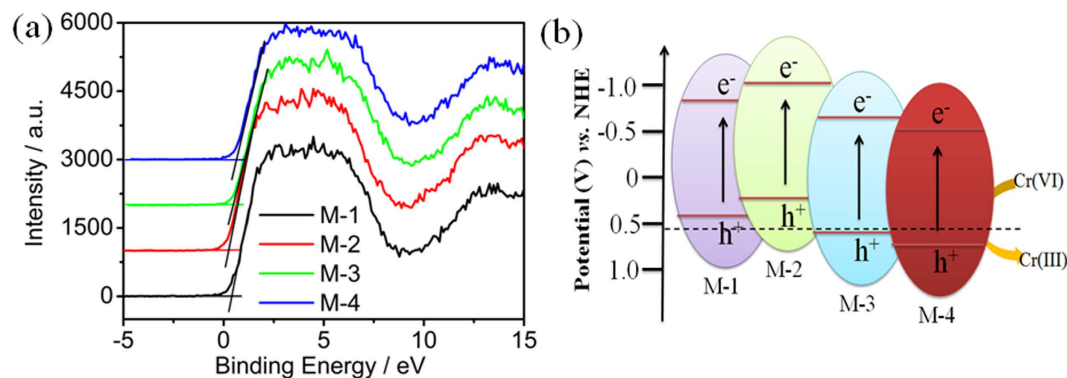
Figure 13. Proposed photocatalytic mechanism for MoSe$_2$ under visible light irradiation.

the CB level of MoSe$_2$ is negative than the Cr(VI)/Cr(III) potential (0.51 V, *vs*. NHE)[48], the photo-generated electrons in MoSe$_2$ can reduce the adsorbed Cr(VI) to produce Cr(III) in the photocatalytic process. Many researches indicate that the Cr(III) species will precipitate on the surface of photocatalyst as Cr$_2$O$_3$ or Cr(OH)$_3$ in the photocatalytic process, which can be removed via simply washing with deionized water or NaOH[49]. Meanwhile, the hole can oxidize the water to form oxygen in the photocatalytic process[50]. Figure S7 shows the O$_2$ evolution yield with irradiation time under visible light irradiation using M-2. It is observed that the O$_2$ evolution yield increases with the increase in the irradiation time, indicating the production of O$_2$ in the photocatalytic process. The major reaction steps are summarized as follows:

$$MoSe_2 + h\nu \rightarrow h^+ + e^-$$

$$Cr_2O_7{}^{2-} + 14H^+ + 6e^- \rightarrow 2Cr^{3+} + 7H_2O$$

$$2H_2O + 4h^+ \rightarrow O_2 + 4H^+$$

Conclusions

MoSe$_2$ samples were successfully synthesized via a facile solvothermal method and their photocatalytic activity in the reduction of Cr(VI) under UV, visible and NIR light irradiation was investigated. The results show that (i) the as-prepared MoSe$_2$ exhibits excellent photo-absorption in the whole light region; (ii) MoSe$_2$ samples display good photocatalytic activity with a Cr(VI) reduction rates of 99%, 91% and 98% at 180 min under UV, visible and NIR light irradiation, respectively; (iii) the enhanced photocatalytic activity is ascribed to the comparatively higher light absorption, efficient charge separation and transfer as well as the relatively large number of surface active sites; (iv) the photo-generated electrons govern this photocatalytic process.

Methods

Preparation of MoSe$_2$.   18 mmol Na$_2$SO$_3$, 4.5 mmol Se power, 2.25 mmol Na$_2$MoO$_4$ and 4.5 mmol NaBH$_4$ were dissolved into 60 ml aqueous solution by sonication for 30 min to produce a uniform dispersion. A dilute HCl solution was dropped in the above solution to adjust the pH value, and the mixture was stirred for 30 min. Subsequently, the mixture was transferred into a 100 ml Teflon-lined stainless steel autoclave, and treated at 150 °C for 12 h. The MoSe$_2$ samples synthesized at pH values of 1, 2, 3 and 4, named as M-1, M-2, M-3 and M-4, were isolated by filtration, washed three times with distilled water, and finally dried in a vacuum oven at 60 °C for 24 h. For the photoelectrochemical testing, 90 mg sample with 0.2 ml 2.5 wt.% polyvinyl alcohol binder was homogenously mixed in water to form slurry. Then, the resultant slurries were coated on the graphite flake (2 cm × 2 cm). Finally, these prepared electrodes were dried in a vacuum oven at 60 °C for 24 h.

Characterization.   The morphology and structure of the samples were characterized by FESEM (Hitachi S-4800), HRTEM (JEOL-2010), XRD (Holland Panalytical PRO PW3040/60) with Cu Kα radiation (V = 30 kV, I = 25 mA), and EDS (JEM-2100). XPS measurement was performed on an Imaging Photoelectron Spectrometer (Axis Ultra, Kratos Analytical Ltd.) with a monochromatic Al Kα X-ray source. The Brunauer-Emmett-Teller specific surface areas of the samples were evaluated on the basis of nitrogen adsorption isotherms measured at 77 K using a BELSORP-max nitrogen adsorption apparatus (Micrometitics, Norcross, GA). The diffuse absorption and reflection spectra of the samples were recorded using a PerkinElmer Lambda750S UV-vis-NIR spectrophotometer equipped with an integrated sphere attachment by using BaSO$_4$ as a reference. PL spectra at room temperature were examined by fluorescence spectrophotometer (HORIBA Jobin Yvon fluoromax-4). The TRPL spectra were obtained on an Edinburgh Lifespec II spectrofluorometer (Edinburgh, UK). Photoelectrochemical measurements were carried out on an electrochemical workstation (AUTOLAB PGSTAT302N) using a three electrode configuration with the as-prepared films as working electrodes, a Pt foil as counter electrode and a standard calomel electrode as reference electrode. The electrolyte was 80 mg l^{-1} Cr(VI) aqueous solution. The

photocurrent measurement was performed at a constant potential of $+0.6\,V$ (*vs.* SCE). 300 W Xe arc lamp ($\lambda > 400\,nm$ and $> 800\,nm$) with a cut off filter and 500 W mercury lamp with a maximum emission at 356 nm were utilized as the light source. EIS were recorded in the frequency range of 0.1 Hz-1 MHz in dark conditions, and the applied bias voltage and ac amplitude were set at open-circuit voltage and 10 mV, respectively.

Photocatalytic experiments.   The photocatalytic activity of the as-prepared samples was evaluated through the experiment of photocatalytic reduction of Cr(VI) under visible and NIR light irradiation. The samples ($1.2\,g\,l^{-1}$) were dispersed in 80 ml Cr(VI) aqueous solutions ($80\,mg\,l^{-1}$) with a pH value of 7 which were prepared by dissolving $K_2Cr_2O_7$ into deionized water. The suspensions were magnetically stirred in the dark for 30 min to reach the adsorption-desorption equilibrium. Under ambient conditions and stirring, the mixed suspensions were exposed to visible and NIR light irradiation produced by a 300 W Xe arc lamp ($\lambda > 400\,nm$ and $> 800\,nm$) with a cut off filter. The light intensity of 300 W Xe arc lamp ($\lambda > 400\,nm$ and $> 800\,nm$) with a cut off filter was approximately 741 and $310\,mW\,cm^{-2}$ measured using a chromameter (CS-100A). A 500 W mercury lamp with a maximum emission at 356 nm and light intensity of $200\,mW\,cm^{-2}$ was used as the UV source for photocatalysis. At certain time intervals, 2 ml of the mixed suspensions were extracted and centrifuged to remove the photocatalysts. The filtrates were analyzed by recording the absorption spectra of Cr(VI) using a PerkinElmer Lambda750S UV-vis-NIR spectrophotometer. The produced gas was analyzed with a gas chromatograph (GC-2014C, Shimadzu, Japan) equipped with a thermal conductivity detector, with N_2 as the carrier gas. A recycled photocatalytic activity test was carried out according to the above-mentioned procedure. After each run of photocatalytic reaction, the fresh Cr(VI) aqueous solution was injected, and the separated photocatalyst was washed with deionized water carefully and used again. To investigate the photocatalytic mechanism, trapping experiments were carried out to determine the main reactive species in the photocatalytic process. The experimental procedure was similar to the photocatalytic activity measurement except that the hole scavengers were added into the reaction system.

References

1. Shen, C. C. *et al.* Superior adsorption capacity of g-C_3N_4 for heavy metal ions from aqueous solutions. *J. Colloid Interface Sci.* **456,** 7–14 (2015).
2. Bhatti, M. S., Reddy, A. S., Kalia, R. K. & Thukral, A. K. Modeling and optimization of voltage and treatment time for electrocoagulation removal of hexavalent chromium. *Desalination* **269,** 157–162 (2011).
3. Liang, R. W., Jing, F. F., Shen, L. J., Qin, N. & Wu, L. MIL-53(Fe) as a highly efficient bifunctional photocatalyst for the simultaneous reduction of Cr(VI) and oxidation of dyes. *J. Hazard. Mater.* **287,** 364–372 (2015).
4. Cao, S. W., Low, J. X., Yu, J. G. & Jaroniec, M. Polymeric Photocatalysts Based on Graphitic Carbon Nitride. *Adv. Mater.* **27,** 2150–2176 (2015).
5. Zhao, J., Han, Q. F., Zhu, J. W., Wu, X. D. & Wang, X. Synthesis of Bi nanowire networks and their superior photocatalytic activity for Cr(VI) reduction. *Nanoscale* **6,** 10062–10070 (2014).
6. Wu, M., Yan, J. M., Tang, X. N., Zhao, M. & Jiang, Q. Synthesis of Potassium-Modified Graphitic Carbon Nitride with High Photocatalytic Activity for Hydrogen Evolution. *ChemSusChem* **7,** 2654–2658 (2014).
7. Zhang, L. *et al.* Preparation of magnetic $Fe_3O_4/TiO_2/Ag$ composite microspheres with enhanced photocatalytic activity. *Solid State Sci.* **52,** 42–48 (2016).
8. Bing, W. *et al.* Visible-light-driven enhanced antibacterial and biofilm elimination activity of graphitic carbon nitride by embedded Ag nanoparticles. *Nano Res.* **8,** 1648–1658 (2015).
9. Bian, J. C. *et al.* Thermal vapor condensation of uniform graphitic carbon nitride films with remarkable photocurrent density for photoelectrochemical applications. *Nano Energy* **15,** 353–361 (2015).
10. Ong, W. J., Tan, L. L., Chai, S. P., Yong, S. T. & Mohamed, A. R. Surface charge modification via protonation of graphitic carbon nitride (g-C_3N_4) for electrostatic self-assembly construction of 2D/2D reduced graphene oxide (rGO)/g-C_3N_4 nanostructures toward enhanced photocatalytic reduction of carbon dioxide to methane. *Nano Energy* **13,** 757–770 (2015).
11. Lv, Y. H., Yao, W. Q., Zong, R. L. & Zhu, Y. F. Fabrication of Wide-Range-Visible Photocatalyst Bi_2WO_{6-x} nanoplates via Surface Oxygen Vacancies. *Sci. Rep.* **6,** 19347 (2016).
12. Li, H. Y. *et al.* Efficiently photocatalytic reduction of carcinogenic contaminant Cr(VI) upon robust AgCl: Ag hollow nanocrystals. *Appl. Catal. B: Environ.* **164,** 344–351 (2015).
13. Liu, X. J. *et al.* Enhanced visible light photocatalytic activity of ZnO doped with downconversion $NaSrBO_3:Tb^{3+}$ phosphors *Dalton Trans.* **44,** 97–103 (2015).
14. Xu, D. F., Cheng, B., Cao, S. W. & Yu, J. G. Enhanced photocatalytic activity and stability of Z-scheme Ag_2CrO_4-GO composite photocatalysts for organic pollutant degradation. *Appl. Catal. B: Environ.* **164,** 380–388 (2015).
15. Di, J. *et al.* Preparation of sphere-like gC_3N_4/BiOI photocatalysts via a reactable ionic liquid for visible-light-driven photocatalytic degradation of pollutants. *J. Mater. Chem. A* **2,** 5340–5351 (2014).
16. Cheng, H. F., Huang, B. B. & Dai, Y. Engineering BiOX (X = Cl, Br, I) nanostructures for highly efficient photocatalytic applications. *Nanoscale* **6,** 2009–2026 (2014).
17. Lv, H. L. *et al.* Enhancement photocatalytic activity of the graphite-like C_3N_4 coated hollow pencil-like ZnO. *J. Colloid Interface Sci.* **450,** 381–387 (2015).
18. Li, Y. J., Yu, L. M., Li, N., Yan, W. F. & Li, X. T. Heterostructures of Ag_3PO_4/TiO_2 mesoporous spheres with highly efficient visible light photocatalytic activity. *J. Colloid Interface Sci.* **450,** 246–253 (2015).
19. Xu, H. F., Li, G., Zhu, G., Zhu, K. R. & Jin, S. W. Enhanced photocatalytic degradation of rutile/anatase TiO_2 heterojunction nanoflowers. *Catal. Commun.* **62,** 52–56 (2015).
20. Zhou, J. *et al.* Growth rate controlled synthesis of hierarchical Bi_2S_3/In_2S_3 core/shell microspheres with enhanced photocatalytic activity. *Sci. Rep.* **4,** 4027 (2014).
21. Ong, W. J., Putri, L. K., Tan, L. L., Chai, S. P. & Yong, S. T. Heterostructured AgX/g-C_3N_4 (X = Cl and Br) nanocomposites via a sonication-assisted deposition-precipitation approach: Emerging role of halide ions in the synergistic photocatalytic reduction of carbon dioxide. *Appl. Catal. B: Environ.* **180,** 530–543 (2016).
22. Ma, L. T. *et al.* Water-assisted ions *in situ* intercalation for porous polymeric graphitic carbon nitride nanosheets with superior photocatalytic hydrogen evolution performance. *Appl. Catal. B: Environ.* **190,** 93–102 (2016).
23. Li, X. F. *et al.* Energy gap engineering of polymeric carbon nitride nanosheets for matching with $NaYF_4:Yb,Tm$: enhanced visible-near infrared photocatalytic activity. *Chem. Commun.* **52,** 453–456 (2016).
24. Hao, Q. *et al.* Aluminum plasmonic photocatalysis. *Sci. Rep.* **5,** 15288 (2015).
25. Xing, M. Y., Li, X. & Zhang, J. L. Synergistic effect on the visible light activity of Ti^{3+} doped TiO_2 nanorods/boron doped graphene composite. *Sci. Rep.* **4,** 5493 (2014).

26. Sun, S. M., Wang, W. Z., Jiang, D., Zhang, L. & Zhou, J. Infrared light induced photoelectrocatalytic application via graphene oxide coated thermoelectric device. *Appl. Catal. B: Environ.* **158–159,** 136–139 (2014).

27. Huang, S. Q. *et al.* Metal recovery based magnetite near-infrared photocatalyst with broadband spectrum utilization property. *Appl. Catal. B: Environ.* **181,** 456–464 (2016).

28. Wang, H. *et al.* Near-Infrared- and Visible-Light-Enhanced Metal-Free Catalytic Degradation of Organic Pollutants over Carbon-Dot-Based Carbocatalysts Synthesized from Biomass. *ACS Appl. Mater. Interfaces* **7,** 27703–27712 (2015).

29. Yu, Y. F. *et al.* Layer-Dependent Electrocatalysis of MoS_2 for Hydrogen Evolution. *Nano Lett.* **14,** 553–558 (2014).

30. Qin, W. *et al.* MoS_2-reduced graphene oxide composites via microwave assisted synthesis for sodium ion battery anode with improved capacity and cycling performance. *Electrochim. Acta* **153,** 55–61 (2015).

31. Chen, Y. J., Tian, G. H., Shi, Y. H., Xiao, Y. T. & Fu, H. G. Hierarchical MoS_2/Bi_2MoO_6 composites with synergistic effect for enhanced visible photocatalytic activity. *Appl. Catal. B: Environ.* **164,** 40–47 (2015).

32. Tan, Y. H. *et al.* The combinations of hollow MoS_2 micro@nano-spheres: one-step synthesis, excellent photocatalytic and humidity sensing properties. *J. Mater. Chem. C* **2,** 5422–5430 (2014).

33. Min, Y. L., He, G. Q., Xu, Q. J. & Chen, Y. C. Dual-functional MoS_2 sheet-modified CdS branch-like heterostructures with enhanced photostability and photocatalytic activity. *J. Mater. Chem. A* **2,** 2578–2584 (2014).

34. Wei, W., Dai, Y. & Niu, C. w. & Huang, B. B. Controlling the Electronic Structures and Properties of in-Plane Transition-Metal Dichalcogenides Quantum Wells. *Sci. Rep.* **5,** 17578 (2015).

35. Shi, Y. F. *et al.* Highly Ordered Mesoporous Crystalline $MoSe_2$ Material with Efficient Visible-Light-Driven Photocatalytic Activity and Enhanced Lithium Storage Performance. *Adv. Funct. Mater.* **23,** 1832–1838 (2013).

36. Zhuang, H. L. & Hennig, R. G. Computational Search for Single-Layer Transition-Metal Dichalcogenide Photocatalysts. *J. Phys. Chem. C* **117,** 20440–20445 (2013).

37. Fan, C., Wei, Z. M., Yang, S. X. & Li, J. B. Synthesis of $MoSe_2$ flower-like nanostructures and their photo-responsive properties. *RSC Adv.* **4,** 775–778 (2014).

38. Etzkorn, J. *et al.* Metal-Organic Chemical Vapor Depostion Synthesis of Hollow Inorganic-Fullerene-Type MoS_2 and $MoSe_2$ Nanoparticles. *Adv. Mater.* **17,** 2372–2375 (2005).

39. Bang, G. S. *et al.* Effective Liquid-Phase Exfoliation and Sodium Ion Battery Application of MoS_2 Nanosheets. *ACS Appl. Mater. Interfaces* **6,** 7084–7089 (2014).

40. Zhang, X. Y. *et al.* Effect of aspect ratio and surface defects on the photocatalytic activity of ZnO nanorods. *Sci. Rep.* **4,** 4596 (2014).

41. Min, S. X. & Lu, G. X. Sites for high efficient photocatalytic hydrogen evolution on a limited-layered MoS_2 cocatalyst confined on graphene sheets-the role of graphene. *J. Phys. Chem. C* **116,** 25415–25424 (2012).

42. Zheng, W. T. & Sun, C. Q. Underneath the fascinations of carbon nanotubes and graphene nanoribbons. *Energy Environ. Sci.* **4,** 627–655 (2011).

43. Liu, X. J. *et al.* Light converting phosphor-based photocatalytic composites. *Catal. Sci. Technol.* **5,** 4727–4740 (2015).

44. Yu, W. *et al.* Enhanced visible light photocatalytic degradation of methylene blue by F-doped TiO_2. *Appl. Surf. Sci.* **319,** 107–112 (2014).

45. Liu, B. *et al.* Hierarchical TiO_2 spherical nanostructures with tunable pore size, pore volume, and specific surface area: facile preparation and high-photocatalytic performance. *Catal. Sci. Technol.* **2,** 1933–1939 (2012).

46. Liu, X. J., Pan, L. K., Lv, T. & Sun, Z. CdS sensitized TiO_2 film for photocatalytic reduction of Cr(VI) by microwave-assisted chemical bath deposition method. *J. Alloys Compd.* **583,** 390–395 (2014).

47. Yu, J. Y. *et al.* Photogenerated electron reservoir in hetero-p-n CuO-ZnO nanocomposite device for visible-light-driven photocatalytic reduction of aqueous Cr(VI). *J. Mater. Chem. A* **3,** 1199–1207 (2015).

48. Wang, X. L., Pehkonen, S. O. & Ray, A. K. Removal of aqueous Cr (VI) by a combination of photocatalytic reduction and coprecipitation. *Ind. Eng. Chem. Res.* **43,** 1665–1672 (2004).

49. Hu, S. W. *et al.* Simultaneous nanostructure and heterojunction engineering of graphitic carbon nitride via *in situ* Ag doping for enhanced photoelectrochemical activity. *Appl. Catal. B: Environ.* **163,** 611–622 (2015).

50. Zhu, G. *et al.* A facile synthesis of ZnO/CNT hierarchical microsphere composites with enhanced photocatalytic degradation of methylene blue. *RSC Adv.* **5,** 72476–72481 (2015).

Acknowledgements

Author Contributions

X.L. and C.S. designed the research, analyzed the data and wrote the manuscript. H.C., B.L., W.L. and J.L. performed the characterization. G.Z., H.D., J.L. and C.L. discussed the results and commented on the manuscript. All authors reviewed the manuscript.

Additional Information

Supplementary information accompanies this paper at http://www.nature.com/srep

Competing financial interests: The authors declare no competing financial interests.

How to cite this article: Chu, H. *et al.* Hexagonal 2H-$MoSe_2$ broad spectrum active photocatalyst for Cr(VI) reduction. *Sci. Rep.* **6,** 35304; doi: 10.1038/srep35304 (2016).